SCIENTIFIC REPORTS

OPEN

SUBJECT AREAS:
RNA
BIOSENSORS
APPLICATIONS OF AFM
DIAGNOSTIC MARKERS

Received
24 April 2013

Accepted
8 August 2013

Published
30 August 2013

Correspondence and requests for materials should be addressed to A.W.N. (anichol@temple.edu) or M.C. (mcastronovo@cro.it)

Digital Imprinting of RNA Recognition and Processing on a Self-Assembled Nucleic Acid Matrix

Shiv K. Redhu[1], Matteo Castronovo[2,3] & Allen W. Nicholson[1,3]

[1]Department of Chemistry, Temple University, 1901 North 13th Street, Philadelphia, PA, 19122, USA, [2]Department of Translational Research - Unit of Experimental and Clinical Pharmacology, CRO - National Cancer Institute, Via Franco Gallini 2, Aviano, PN, I-33081, Italy, [3]Department of Biology, Temple University, 1900 North 12th Street, Philadelphia, PA, 19122, USA.

The accelerating progress of research in nanomedicine and nanobiotechnology has included initiatives to develop highly-sensitive, high-throughput methods to detect biomarkers at the single-cell level. Current sensing approaches, however, typically involve integrative instrumentation that necessarily must balance sensitivity with rapidity in optimizing biomarker detection quality. We show here that laterally-confined, self-assembled monolayers of a short, double-stranded(ds)[RNA-DNA] chimera enable permanent digital detection of dsRNA-specific inputs. The action of ribonuclease III and the binding of an inactive, dsRNA-binding mutant can be permanently recorded by the input-responsive action of a restriction endonuclease that cleaves an ancillary reporter site within the dsDNA segment. The resulting irreversible height change of the arrayed ds[RNA-DNA], as measured by atomic force microscopy, provides a distinct digital output for each dsRNA-specific input. These findings provide the basis for developing imprinting-based bio-nanosensors, and reveal the versatility of AFM as a tool for characterizing the behaviour of highly-crowded biomolecules at the nanoscale.

An important goal of basic and translational research is the ability to achieve accurate, high-throughput detection of biomolecules in single-cell amounts[1,2]. The inherent capacity of nucleic acids to self-assemble provides an essential foundation for developing novel methods to detect biomarkers in micro-samples, as it permits the spontaneous formation of nucleic acid nanostructures with programmable density and functionality[3–5]. Coupled with atomic force microscopy (AFM) that allows topographic imaging and compressibility measurement, nucleic acid nanostructures on flat, solid supports enable assays of ligand binding with single molecule detection capability[5–7]. AFM also can be used more broadly for the label-free, amplification-independent detection of a range of biomolecules in confined assemblies[7–11], and can detect changes in topography and elasticity of surface-bound molecules in response to specific inputs[7,12]. In detecting disease-related biomarkers, current AFM-based approaches typically rely on direct visualization of surface-captured target biomolecules that remain at fixed positions as the AFM signals are collected[7,8,10]. Recently developed scanning-probe instrumentation can reliably achieve the rapid imaging of biological surfaces with molecular resolution, at speeds approaching one frame per several tens of msec[13–15].

Roukes and co-workers[2] compared the performances of several nano-biosensors and found that the observed sensitivity for a given protein biomarker negatively correlates with the analysis time. This is consistent with the fact that achievement of a robust output with single-cell sensitivity requires cascade-based amplification, involving labelled probes and/or targets[1,3,5]. Moreover, the analysis of single-cell quantities of biomarkers requires complex, time-consuming sample preparation which adds steps to the detection process, which in turn can lead to increased noise and sample degradation[1,16]. Nucleic acid detection methodologies have largely led the nanobiosensor field, not only because of the importance of nucleic acids as biomarkers, but also because the molecules can be specifically recognized, processed, or amplified by many enzymes. Moreover, nucleic acids can interact with opportunely designed probes, forming complex structures with controllable architectures and diverse functions. In addition, several sensor schemes can detect nucleic acid targets by using nucleic acid probes as imprinting agents, following target-probe recognition[5]. This approach allows the recording of target-related information on easy-to-access supports, which can be subsequently analysed. Similar approaches have not yet been systematically established with proteins, as it has mainly involved formation and detection of difficult-to-control antigen-antibody molecular complexes.

AFM studies have shown that nanopatches of self-assembled monolayers of double-stranded(ds) DNA, typically containing ~10^5 molecules, and formed by an AFM-based nanomanipulation approach termed nanografting[17–20] (see Fig. 1a, and Supplementary Fig. S1) can be processed by restriction endonucleases. The reaction can be recorded by a permanent height change of the nanopatch, reflecting the significant shortening of the inherently rigid, surface-bound dsDNA molecules[21,22]. It also was shown that enzyme access to a dsDNA nanopatch can be sterically regulated, as revealed by a progressive decrease in reactivity as a function of increasing dsDNA density[21–23]. These results in turn suggested that the sterically-responsive accessibility of a dsDNA nanopatch towards a restriction enzyme could be exploited to develop a novel nanosensor, able to detect the binding of target molecules that cause an alteration in accessibility[24].

In this study we establish for the first time a single-step, label-free approach to detect biomolecules that bind and/or process dsRNA, using a nanomanipulated, self-assembled monolayer (SAM) of a rigid ds[RNA-DNA] chimera as imprinting matrix; a reference nuclease as imprinting agent; and AFM for imprint-readout. We specifically chose a surface-bound, dsRNA-containing probe because the ability to detect and characterize dsRNA and/or dsRNA-related biomolecules in small (e.g. single-cell) volumes would be of significant value for diagnostic and functional genomic studies. In this regard, dsRNA is a biomarker for specific cancers[25–27] and viral infection[28–30]. dsRNA also is a conserved structural feature of precursors to gene-regulatory RNAs[31–34] including miRNAs and siRNAs[35,36]. In addition, a single molecule of dsRNA is sufficient to trigger the cellular interferon response[37].

Results

The experimental approach involved the design of a prototypical target (or probe) dsRNA in the form of a 39 bp ds[RNA-DNA] chimera, containing a cleavage site within the dsRNA segment for the dsRNA-specific enzyme, ribonuclease III (RNase III)[38] and a cleavage site for restriction endonuclease BamHI within the DNA segment. RNase III is a conserved bacterial endoribonuclease that participates in the maturation of diverse RNAs, including the 16S and 23S ribosomal RNAs. RNase III requires Mg^{2+} for catalytic activity, and can specifically recognize and cleave its cellular substrates *in vitro* at sites that are identified by preferred bp sequence elements[38]. The site-specific cleavage of the dsRNA segment by RNase III would shorten the duplex by 16 bp (see schematic, Fig. 1a top right, and the dsRNA-binding sequence, framed in red, with the cleavage sites indicated by red arrows in Fig. 2a), while BamHI cleavage of the dsDNA segment, proximal to the surface to which the ds[RNA-DNA] is attached, would provide a 4 bp product (see dsDNA restriction site framed in blue in Fig. 2d). Supplementary Fig. S1 shows that ds[RNA-DNA] matrices can be formed in different ways. In Fig. 1a, the duplex is prepared by annealing the complementary ss[RNA-DNA] strands in solution, then affixing the duplex structure to a gold surface *via* an alkylthiol linker, forming

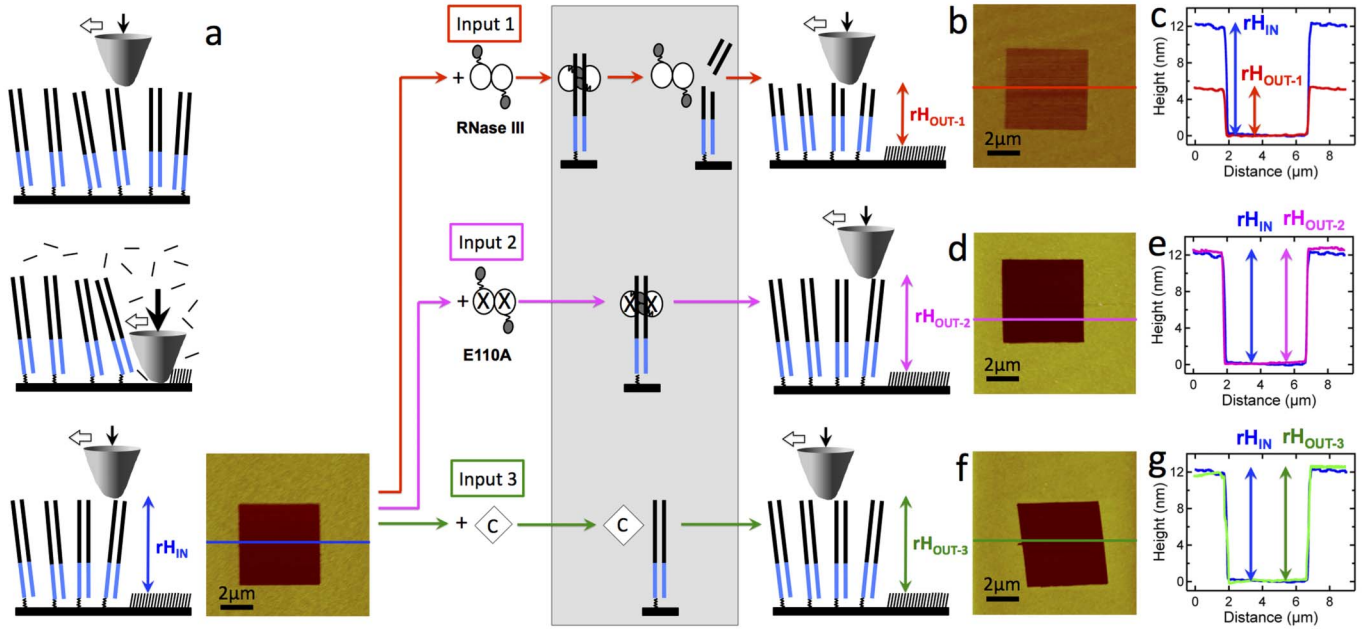

Figure 1 | AFM-based nanopatterning of a ds[RNA-DNA] matrix, and detection of recognition and processing. Shown are the results of different Inputs on the height of the ds[RNA-DNA] matrix, as measured by AFM. (a) depicts the nanografting process used to form a laterally-confined ds[RNA-DNA] matrix (bottom-left) starting from a self-assembled monolayer of a preformed ds[RNA-DNA] chimera (top-left). In the centre-left display, the AFM tip at high force (~100 nN) displaces ds[RNA-DNA] molecules, which are replaced by molecules of the ethylene-glycol-terminated alkylthiol, TOEG6 (see Methods), thereby forming a pit that provides lateral confinement to the ds[RNA-DNA] monolayer. The bottom-centre displays an AFM micrograph of the ds[RNA-DNA] matrix. The chimeric duplex structure contains a short thiol linker, a dsDNA segment (schematically depicted in blue) and a dsRNA segment (depicted in black) (see also Supplementary Fig. S1). The ds[RNA-DNA] matrix also contains a rectangular pit consisting of a nanografted patch of monolayer of TOEG6 (see Methods). The estimated ds[RNA-DNA] density is ~10^4 molecules μm^{-2} (see Methods). (b) shows an AFM micrograph of the ds[RNA-DNA] matrix shown in (a), following RNase III treatment (Input 1). Putative reaction intermediate states are highlighted in grey on the left (see also Fig. 2a). The graph in (c) shows the side-by-side height profiles of the ds[RNA-DNA] matrix before (rH_{IN} in a) and after (rH_{OUT-1} in b) RNase III treatment. RNase III cleavage of dsRNA is demonstrated by a 2-fold height decrease. (d) displays an AFM micrograph of the ds[RNA-DNA] matrix after treatment with the catalytically inactive E110A RNase III mutant (Input 2). The putative intermediate reaction state is highlighted in grey on the left (see also Fig. 2a). In (e) the height profiles are essentially the same, indicating that the catalytic action of RNase III is required for the height decrease observed in (c). (f) and (g) show that a control experiment (omitting RNase III; open diamond, Input 3) provides the same AFM topographic profiles as shown in (d) and (e). A "brighter is higher" colour code is used for the AFM topographic micrograph in (b), (d), and (f).

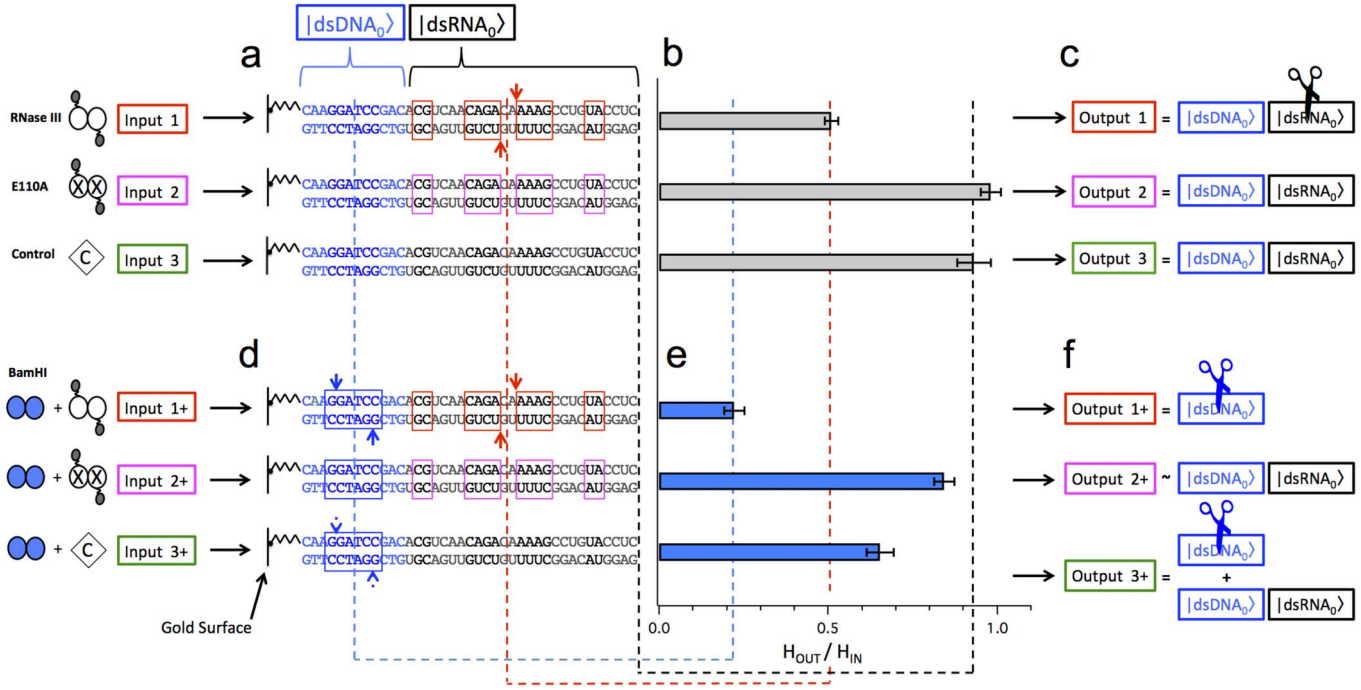

Figure 2 | Digital imprinting of dsRNA recognition and processing on a ds[RNA-DNA] matrix. Shown in (a) and (d) is the sequence of the 39-bp ds[RNA-DNA] (12-bp of dsRNA, 27-bp of dsDNA), containing an *A. aeolicus* RNase III processing site positioned in the middle of the dsRNA segment (|dsRNA$_0$⟩). The dsRNA sequence corresponds to the duplex stem in the *A. aeolicus* 23S rRNA precursor[38]. The red rectangles indicate sites of enzyme contact[38], and the scissile phosphodiesters are indicated by the red arrows. (a) Input 1 (red): RNase III cleavage of the target site would create a surface-attached, 23-bp ds[RNA-DNA] with a 2-nt, 3′-overhang terminus (calculated length ~7.1 nm). Input 2 (magenta), uses the RNase III E110A mutant, which retains dsRNA-binding ability[31,39]. This input does not alter the height, and is essentially identical to the control experiment that omits RNase III (Input 3: green) (see also Table 1). (b) The H_{OUT}/H_{IN} value indicates that Output 1 corresponds to a ds[RNA-DNA] that is processed by RNase III (red dashed line), whereas Outputs 2 and 3 correspond to an unaltered dsDNA-dsRNA segment (black dashed line). (c) schematically depicts the output matrices [1–3], in which [1] consists of a monolayer of duplexes comprising the unaltered |dsDNA$_0$⟩ segment and a cleaved |dsRNA$_0$⟩ segment. The structures in (d) highlight the BamHI recognition sequence (enclosed in blue rectangles). BamHI action would create a surface-bound, 4-bp product possessing a 4-nt 3′-overhang (calculated length ~1.4 nm). In (e), three distinct 'imprints' are generated when BamHI is included (Inputs 1+–3+). For Input 1+, the ds[RNA-DNA] is processed at the BamHI site (blue dashed line), when RNase III also is present. For Input 3+, BamHI displays only limited catalytic action in the absence of RNase III, while for Input 2+, BamHI is inhibited in the presence of the E110A RNase III mutant (note error bars for Outputs 2+ and 3+). (f) schematically depicts the output matrices [1–3+], in which [1+] consists of a monolayer of duplexes comprising the cleaved |dsDNA$_0$⟩ segment, and [3+] consists of a mixed monolayer of cleaved |dsDNA$_0$⟩ segments and intact duplexes. Data are means, including the standard deviations.

a self-assembled monolayer (see top left in Fig. 1a)[22]. Subsequent nanografting of an inert, bioresistant alkylthiol (see also Methods section) provides a "pit" (see centre left in Fig. 1a) as a reference point for measurement of relative height (rH_{IN}) on the monolayer (see bottom left in Fig. 1a, and also supplementary Fig. S1b–c).

Table 1 summarizes the different treatments of the ds[RNA-DNA] matrices, as follows. Topographic AFM images of a ds[RNA-DNA] matrix, before and after RNase III treatment (defined as Input 1: see Table 1, and top right in Fig. 1a), are shown in Fig. 1a (bottom-centre) and 1b, respectively. The corresponding line profile (shown in blue in Fig. 1c) establishes an initial height of 12 nm for the ds[RNA-DNA] matrix (shown in Fig. 1a, bottom-centre) with respect to the reference alkylthiol SAM (Fig. 1c, rH_{IN}; blue arrow), and a height of 5 nm following RNase III treatment (Fig. 1c, rH_{OUT-1}; red arrow). Input 2 (see centre right in Figure 1a) represents the action of the E110A RNase III mutant, which is catalytically inactive but retains dsRNA-binding capability[31,39] (see dsRNA-binding sequence framed in magenta in Fig. 2a). The essentially identical line profiles before and after treatment (Fig. 1e), demonstrate that only the catalytically active form of RNase III (Input 1) provides a permanent height change. Input 3 in Fig. 1a (bottom-right) refers to different control experiments (see Table 1), including incubation in buffer without enzyme, or including RNase III but omitting the catalytic cofactor Mg^{2+} (see line profile in Fig. 1g). Although Input 2 is expected to involve an intermediate state that is qualitatively distinct from that of Input 1 (highlighted in grey in Fig. 1a), it cannot be distinguished from the control experiments (Input 3) because the outputs are identical (compare rH_{OUT-2} in Fig. 1e and rH_{OUT-3} in Fig. 1g). However, Input 2 can be distinguished from Input 3 by the use of an ancillary reporter enzyme (see below). The absolute height values of the matrix H_{IN} and H_{OUT} can be derived from the AFM-measured, relative height values rH_{IN} and rH_{OUT}, respectively (see Methods section). The histogram of H_{OUT}/H_{IN} for the three inputs described above is shown in Fig. 2b, and summarizes the results obtained with ds[RNA-DNA] matrices having a relative initial height as shown in Fig. 1c (rH_{IN}; blue arrow). The histogram shows that the ds[RNA-DNA] matrix is a sensor of the catalytic action of RNase III by providing a distinct, AFM-readable change in matrix height (for each input, see schematic representation of the matrices after treatment in Fig. 2c).

The combination of RNase III and BamHI (Input 1+) produces an output that is qualitatively distinct from that of RNase III alone (Input 1) (compare Fig. 2b and 2e, relative to Input 1 and 1+ respectively). The H_{OUT}/H_{IN} ratio obtained with combined enzyme (Output 1+) is significantly lower than the value obtained with RNase III alone (Output 1), and is consistent with cleavage of the

Table 1 | Experimental conditions used for enzymatic reactions on ds[RNA-DNA] matrices. Input 1 experiments (see Fig. 1–3), were conducted using two different enzyme concentrations (30 or 100 nM RNase III), which provided equivalent results. The experiments relevant to Input 3+, and with an $H_{IN} > 11$ nm, were conducted using the standard RNase III reaction buffer. See Methods for complete description of reaction conditions

	Input 1		Input 2		Input 3		Input 1+		Input 2+		Input 3+	
RNase III	100 nM	30 nM	-	-	100 nM		100 nM		-	-	-	
E110A	-	-	100 nM	-	-		-		100 nM	-	-	
BamHI	-	-	-	-	-		0.2 U/μl		0.2 U/μl	0.2 U/μl	0.2 U/μl	
$MgCl_2$	15 mM	15 mM	15 mM	15 mM	-		15 mM		15 mM	15 mM	10 mM	
NaCl	50 mM	50 mM	50 mM	50 mM	50 mM		50 mM		50 mM	50 mM	100 mM	
Reaction buffer	30 mM Tris-HCl	30 mM Tris-HCl	30 mM Tris-HCl	30 mM Tris-HCl	30 mM Tris-HCl		30 mM Tris-HCl		30 mM Tris-HCl	30 mM Tris-HCl	50 mM Bis-Tris-HCl	
BSA	-	-	-	-	-		~20 nM		~20 nM	~20 nM	~20 nM	
pH	8	8	8	8	8		8		8	8	6	
T	40°C	40°C	40°C	40°C	40°C		40°C		40°C	40°C	25°C	
Reaction time	2 h 30′	2 h 30′	2 h 30′	2 h 30′	2 h 30′		2 h 30′		2 h 30′	2 h 30′	2 h 30′	
Washing 2	50 mM NaCl TE	50 mM NaCl TE	50 mM NaCl TE	50 mM NaCl TE	50 mM NaCl TE		50 mM NaCl TE		50 mM NaCl TE	50 mM NaCl TE	50 mM NaCl TE	
Washing 3	-	-	-	-	-		NEB4-buffer		NEB4-buffer	NEB4-buffer	NEB4-buffer	
Washing 4	1 M NaCl TE	1 M NaCl TE	1 M NaCl TE	1 M NaCl TE	1 M NaCl TE		1 M NaCl TE		1 M NaCl TE	1 M NaCl TE	1 M NaCl TE	

ds[RNA-DNA] duplex at the BamHI site (see Fig. 2d schematic; blue arrows), creating a 4 bp, surface-attached product (see schematic representation of the output matrix [1+] in Fig. 2f, and compare it with the output matrix [1] in Fig. 2c). In contrast, for BamHI alone (Input 3+), the H_{OUT}/H_{IN} (Output 3+) is significantly higher than that of RNase III alone (Output 1). Since matrix height is determined by ds[RNA-DNA] length, and since the duplex has a single BamHI recognition site, it is likely that the output for BamHI alone reflects an inefficient reaction that leaves a significant number of unmodified duplexes in the matrix (see schematic of the Output matrix [3+] in Fig. 2f, which represents a mixed monolayer of cleaved and unmodified duplexes, and compare with the output matrix [3] in Fig. 2c). In contrast, when the E110A RNase III mutant is included in the BamHI reaction (Input 2+), the Output (2+) reflects an essentially fully intact ds[RNA-DNA] matrix. Here, the binding of the E110A RNase III mutant to the dsRNA portion of the ds[RNA-DNA] structure results in substantial inhibition of BamHI access to its site (see schematic representation of the output matrix [2+] in Fig. 2f, and compare with the output matrix [2] in Fig. 2c). These results show that BamHI access to its site is responsive to the type of reaction at the dsRNA segment (i.e. phosphodiester cleavage, or protein binding).

The height of a dsDNA monolayer is proportional to its density[21,22]. The question thus arises whether the outputs observed in this study also exhibit a similar dependence on monolayer density. Fig. 3a shows the output from Input 1 as a function of ds[RNA-DNA] matrix density, as qualitatively gauged by initial height (H_{IN}). Specifically, an H_{IN} of >11.5 nm corresponds to the maximum height calculated for a near-vertical orientation of the molecules (see also Discussion), reflecting the near-maximal density of the ds[RNA-DNA] matrix. Output 1 (Fig. 3a, solid red triangles) shows that the change in height of the ds[RNA-DNA] matrix linearly correlates with H_{IN}, indicating that the RNase III cleavage site remains accessible, regardless of density. When BamHI is included, the results (Output 1+; Fig. 3a, open triangles) show that the dsDNA segment is accessible to BamHI in the presence of RNase III, also regardless of density. A requirement for the prior action of RNase III for the BamHI reaction is likely, since the same results are obtained if the ds[RNA-DNA] matrix is pretreated with RNase III, then incubated with BamHI following removal of RNase III (data not shown). In contrast, the action of BamHI is inefficient when the relatively dense ds[RNA-DNA] matrix ($H_{IN} > 10$ nm) does not receive prior treatment with RNase III (Output 3+, Fig. 2d; open diamonds). Finally, BamHI action is fully suppressed in the presence of the E110A mutant, regardless of matrix density (Output 2+, open circles). The results shown in Figs. 2 and 3 indicate that BamHI action exhibits a dependence on RNase III catalytic action (+RNase III) or RNase III binding (+E110A) that occurs in the dsRNA segment. Thus, BamHI can effectively capture either a catalytic or noncatalytic RNA-protein interaction by generating a specific, permanent, AFM-readable matrix imprint.

The height of the ds[RNA-DNA] matrix, as well as the imprinting process, also are responsive to small molecule interactions. The binding of ethidium cation to the ds[RNA-DNA] is directly demonstrated by fluorescence enhancement (Fig. 4a) as well as increased height (Fig. 4b), both of which are consistent with intercalation of the planar cation into the surface-bound duplex structures. As additional support for an intercalative process, the height of the corresponding ss[RNA-DNA] matrix is not altered by ethidium, nor is there a significant increase in fluorescence (see right hand side of Fig. 4b). It was shown that the ethidium inhibits RNase III through dsRNA intercalation[40]. The addition of ethidium to the ds[RNA-DNA] matrix blocks the action of RNase III, as well as BamHI, as revealed by suppression of the imprint ($H_{IN} = H_{OUT} = 13.1 \pm 0.5$ nm; data not shown).

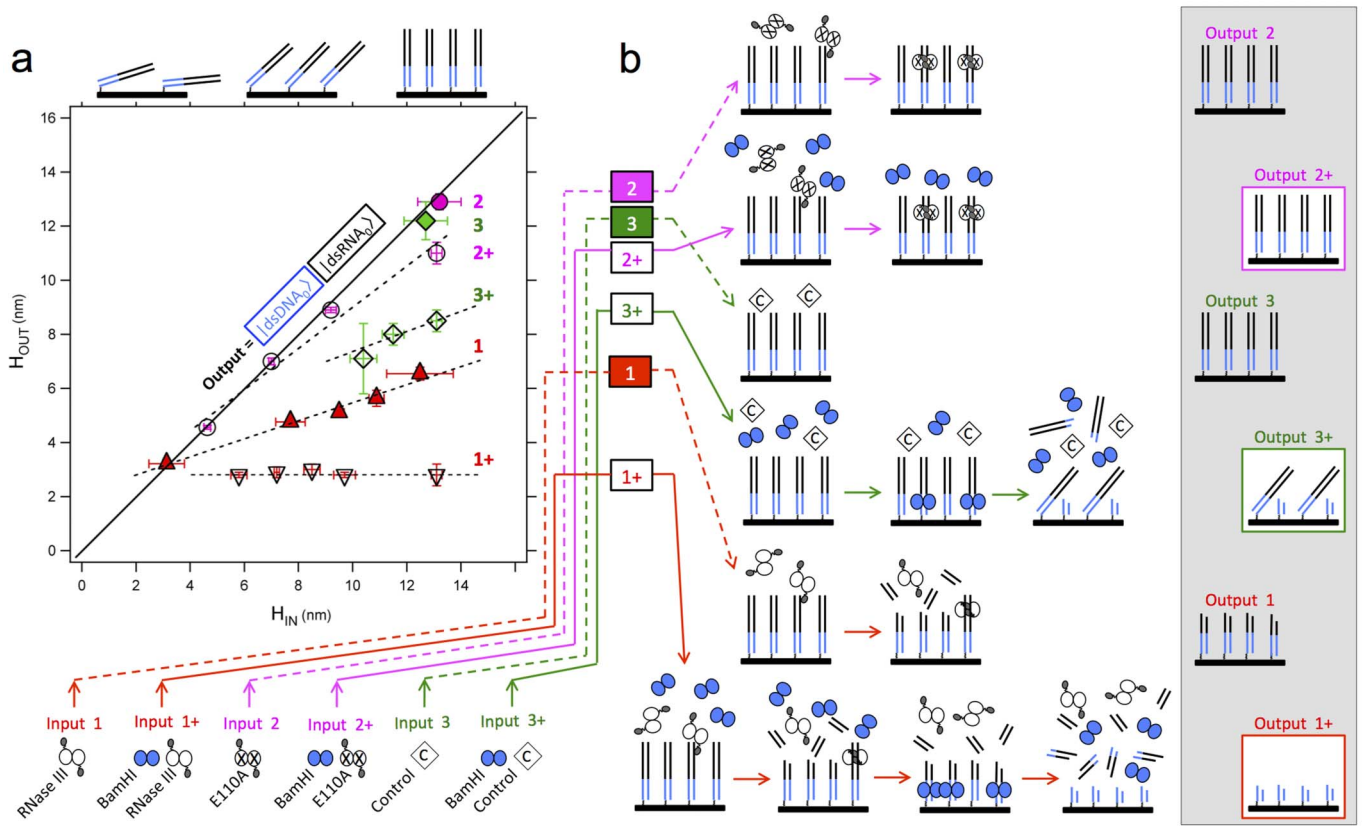

Figure 3 | Density-dependent steric regulation of imprinting a ds[RNA-DNA] matrix. (a) The final heights (H_{OUT}) of six separate Inputs are dependent upon the initial height (H_{IN}) of the ds[RNA-DNA] matrix. ▲ Input 1 (with RNase III). ● Input 2 (with E110A). ◆ Input 3 (controls, either lacking RNase III or with RNase III without the catalytic cofactor, Mg^{2+}). ▽ Input 1+ (with RNase III and BamHI). ○ Input 2+ (with E110A and BamHI). ◇ Input 3+ (with BamHI alone). All dashed lines in (a) relate the data points to a linear regression. The data for Output 1 show that RNase III can process the dsRNA segment regardless of ds[RNA-DNA] density, which is related to the initial height (see schematic representation on top). Outputs 2 and 3 are consistent with an unaltered ds[RNA-DNA] chimera (represented by the solid diagonal line: $H_{OUT} = H_{IN}$). BamHI gains full access to its site in combination with RNase III (Output 1+) as $H_{OUT\ 1+} \ll H_{OUT\ 1}$, while it is essentially completely blocked in combination with the E110A mutant (Output 2+) as $H_{OUT\ 2+} \sim H_{IN}$. BamHI restriction enzyme efficiency acting alone (Input 3+) must be lower than that of RNase III alone (Input 1), as the height of an matrix consisting of ds[RNA-DNA] molecules cleaved by BamHI would be lower than the height of an matrix cleaved by RNase III, and, in contrast, $H_{OUT\ 3+} > H_{OUT\ 1}$ for relatively dense matrices ($H_{IN} > 10$ nm). Data are means, and include standard deviations. (b) Schematic depiction of the effect of different inputs on a highly dense ds[RNA-DNA] matrix, including a steric hindrance-based model that shows how the 'imprint' (Output n+) is a step (i.e. digital) function of Input n+ (n = 1,3), as shown in (a).

Discussion

The results shown in Fig. 3a collectively indicate that for an initial condition of $H_{IN} > 10$ nm, BamHI action in a dense nucleic acid matrix is subject to steric regulation, since the reaction is more efficient in a matrix that contains shortened duplexes, but is inhibited in the presence of the dsRNA-binding E110A RNase III mutant, regardless of matrix density. This behaviour is consistent with the previous observation that the accessibility of a dsDNA monolayer to a restriction endonuclease is dependent upon dsDNA density[21,22]. The density-independent RNase III reactivity of the ds[RNA-DNA] monolayer used in this study may reflect the ability of the two C-terminal dsRNA-binding domains (dsRBDs) of the homodimeric RNase III to engage dsRNA in a sequence-independent manner[38]. Thus, an initial engagement of either dsRBD to a solvent-exposed dsRNA segment may allow the enzyme to access the otherwise sequestered cleavage site. Since BamHI lacks an analogous domain, and since it also is incapable of recognizing dsRNA[41], it cannot easily access its recognition site *via* one-dimensional diffusion along the ds[RNA-DNA] chimeric structure[42]. The results termed Output 2+ (see Fig. 3a, open circles) suggest that, upon dsRBD-dependent binding of the E110A RNase III mutant to the dsRNA segment, the action of BamHI on the dsDNA segment is subject to inhibition by a steric mechanism. The hindrance may specifically occur proximal to the dsDNA segment, as upon E110A binding the limited space available to BamHI would prohibit stable binding. Alternatively, the average molecular density in the matrix following E110A addition may exceed a specific threshold, thereby blocking access of BamHI to the matrix altogether (see schematic representation of proposed surface processes that link Inputs 1–3, and 1–3+ to the corresponding outputs, at the bottom in Fig. 3a, and in Fig. 3b). Regardless of the exact mechanism, these results, together with the data presented in Fig. 2d, show that BamHI is a sensitive indicator of steric hindrance in the ds[RNA-DNA] matrix.

Using AFM-based approaches we have shown that a laterally-confined, self-assembled monolayer consisting of a double-helical RNA-DNA chimera exhibits nuclease reactivity that is subject to catalytic, steric, and small molecule regulation. Using the sequence-specific BamHI endonuclease as a standardized lithographic tool, permanent imprints can be generated on the ds[RNA-DNA] matrix. AFM-readable nucleic acid matrices need only be several microns in diameter, involving several thousand ds[RNA-DNA] molecules, and the imprints can be readily detected by AFM imaging in biologically compatible aqueous buffers. The change in matrix height allows label-free identification of interactions of the surface-exposed dsRNA segment with the different inputs, including an RNA processing nuclease, an RNA-binding

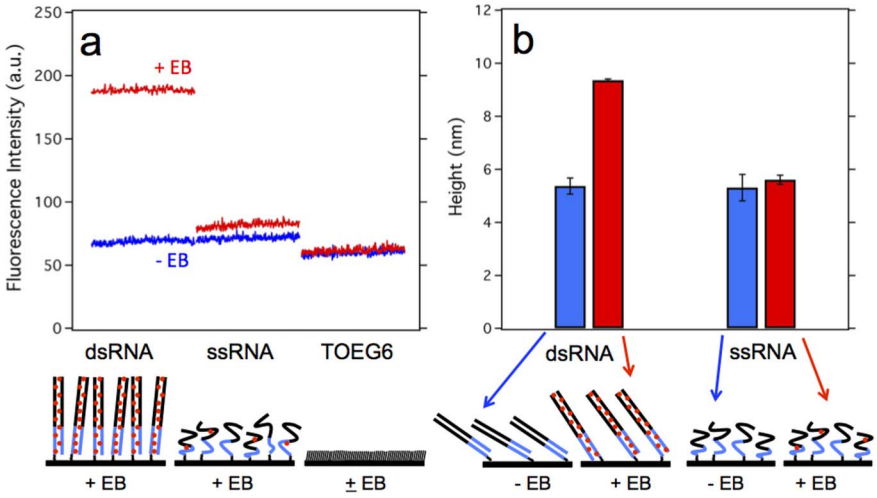

Figure 4 | Detection of ethidium intercalation in a ds[RNA-DNA] matrix. Shown are the effects of ethidium bromide (EB) on the ds[RNA-DNA] matrix, as measured by fluorescence microscopy and by AFM. (a) Fluorescence analysis. Prior to EB addition, the ds- and ss[RNA-DNA] matrices display only nominal (background) fluorescence (shown in blue). Upon EB addition, followed by a single wash (see Methods), the fluorescence intensity (shown in red) specifically increases for the ds[RNA-DNA] matrix. The fluorescence intensity is measured in arbitrary units (au). (b) AFM analysis. Prior to EB addition, the ds- and ss[RNA-DNA] matrices display the same AFM imprint (shown in blue, as measured by height). Here, the initial heights for the two matrices are similar, as the inherent densities are non-identical. Upon EB addition, followed by a single wash, the topographic height (in red) specifically increases for the ds[RNA-DNA] matrix. Data are means, with standard deviations.

protein, and an intercalating agent. The retained functionality of the ds[RNA-DNA] chimera in the matrix environment is revealed by the catalytic action of RNase III, which causes a decrease in matrix height (see Fig. 1c and Output 1 in Fig. 2c). Also, the data displayed in Fig. 3a show that RNase III action within the ds[RNA-DNA] matrix is essentially independent of steric constraints.

Despite the use of extended reaction times and a relatively high (nM) concentration of enzyme, BamHI alone produces only a limited amount of processed ds[RNA-DNA] molecules (see schematic representations of Output 3+ in Figs. 2f and 3b), and is essentially fully inhibited in the presence of the E110A RNase III mutant (see Output 2+ in Figs. 2f and 3b). These results suggest that (i) BamHI access to its site is limited in ds[RNA-DNA] matrices that contain molecules exhibiting near-vertical orientations, and (ii) the binding of the E110A RNase III mutant to the dsRNA segment of the ds[RNA-DNA] structure prevents BamHI access to the contiguous dsDNA sequence. Conclusion (i) is consistent with previous studies on the action of restriction endonucleases in dense nanopatches of dsDNA molecules with near-vertical orientations[21,22,24], and conclusion (ii) establishes the ability of protein-RNA binding to create an effective steric barrier to target site access by a second nuclease.

The ds[RNA-DNA] matrices are stable, as AFM imaging can be performed several hours after the input-containing solution is washed from the matrix, and the process can be repeated several times without a change in output. Furthermore, the initial height (H_{IN}) of the ds[RNA-DNA] matrix is highly reproducible (see Methods), and a single AFM imaging run is sufficient to reliably determine the input-dependent change in matrix height. While the sensitive and reliable analysis of disease-associated RNAs remains an important goal in nanomedicine and diagnostics, AFM-based approaches have not been systematically pursued, in part due to concerns about RNA stability, and the lack of data on the physical properties and behaviour of RNA in confined nanoassemblies[19,20,24,43–47]. While AFM-based studies have described the mechanical properties of dsDNA monolayers, there is essentially no information on ssRNA or dsRNA monolayers. For a dsDNA monolayer, the maximum height as measured by AFM equals the calculated length of the molecule[19–22]. In contrast, Fig. 3a shows that the AFM-measured maximum height of a ds[RNA-DNA] monolayer is ~13 nm, which is ~1.5 nm greater than the calculated length of a 27 bp dsRNA segment (~7.5 nm) joined to a 12 bp dsDNA segment (~4.0 nm). In contrast to the various families of double-helical DNAs, dsRNA is structurally conservative, and exhibits an A-form helix with an 11-fold pitch[48]. The double-helical chimera therefore may possess an atypical structure at the dsRNA-dsDNA junction that extends into the flanking segments. Furthermore, dsRNA and dsDNA exhibit different hydration and charge screening patterns[43,48], which may contribute to differing topographic heights of highly dense dsRNA and dsDNA monolayers, as detected by AFM at low loads. Nonetheless, the overall double-helical form of the surface-bound [RNA-DNA] is preserved, as demonstrated by the results shown in Fig. 1–3, as well as the height increase caused by the binding of ethidium, consistent with an intercalative reaction involving a double-helical structure (Fig. 4).

Compared to other nucleic acid-based methods of protein detection, the matrices described here can distinguish dsRNA-binding (Input 2+, see Fig. 3a) from non-binding inputs (including the controls defined by Input 3+; see Fig. 3a) without the need, for example, for engineered probes that undergo a reversible shift in structural equilibrium (e.g., as with molecular switches) upon specific binding[5,49]. Instead, the AFM-readable outputs depend only on the irreversible action of BamHI as a function of dsRNA-specific inputs, using dense monolayers comprised of several thousand molecules. The length and density of the relatively simple (and thus easily-prepared) nucleic acid probes can be varied to match the experimental requirements[24].

The detection sensitivity of the approach described in this work is dependent upon the lateral dimensions of the ds[RNA-DNA] matrix. Starting with a bioresistant monolayer, nanografting can create a monolayer nucleic acid matrix with lateral dimensions ranging from a few microns down to several tens of nanometers[50] (see supplementary Fig. S1h–k). Thus, the smallest nanografted matrix may be expected to contain several hundred copies of the nucleic acid probe. The small size of the sensing element therefore could allow saturable binding of a low-abundance biomarker derived from only several cells, without the need for cell culture.

The data of Fig. 3a that relates the dependence of action of BamHI on the presence or absence of the E110A RNase III mutant (2+, open

circles) suggest that our approach can be applied to the detection of small ssRNAs (e.g. miRNAs). Here, a surface-bound chimera probe, consisting of a thiol-linked dsDNA segment containing a BamHI site and a ssRNA sequence complementary to the target RNA. When the target RNA hybridizes to the probe, a dsRNA segment forms, which can be recognized by the E110A mutant protein, and therefore inhibit the action of BamHI. The implementation of arrays of such matrices could be achieved with standard surface lithography, combined with nucleic acid self-assembly[51,52]. Alternatively, Scoles and co-workers demonstrated that nanografting can provide prototypical nanoarrays of several different ssDNA probes which, following attachment, retain the capacity for sequence-specific hybridization[53].

Using piezo-actuated, gold-coated micropillars and ssDNA self-assembly, Melli *et al.*[54] have demonstrated that the hybridization kinetics of ssDNA on a monolayer patch that is located on top of a micropillar and is only several microns in width, is significantly faster than that observed with the corresponding regular (i.e. flat) SAM[55]. The authors explain that the slower kinetics of the regular SAM predominantly reflects diffusion-limited ssDNA hybridization and the resultant sub-coverage of the surface monolayer patch. A similar behaviour is expected to apply to the ds[RNA-DNA] patch, and suggests that the methodology described in the study of Melli et al. can be applied to the creation of nanoarrays containing diverse probes. Our approach, for example, could be coupled to pillar-based (and related) technologies for detection of nucleic acid-binding proteins exhibiting a range of affinities, since input-specific, permanent imprints would cause permanent, input-specific changes in the mass of the pillar-attached matrices, which in turn provide a permanent, detectable, input-specific shifts in the resonance frequency of the pillar.

In conclusion, the recognition and processing of dsRNA can be permanently recorded on a nanostructured, self-assembled, nucleic acid-based matrix through the use of a well-characterized endonuclease as an imprinting tool. The approach is intrinsically label-free and has the potential to minimize sample degradation induced by AFM imaging, or as a result of time-consuming sample preparation. It is envisioned that this approach will be combined with functional nucleic acid analysis and high-throughput surface lithography for future application in disease diagnostics.

Methods

Preparation of ultra-flat gold surfaces. Ultra-flat gold surfaces were prepared essentially as described elsewhere[20–22]. Briefly, a gold-on-mica sheet (clear ruby muscovite, Mica New York Corp.) was cut into small squares of several millimeters in dimension. The cleaned silicon wafer (no special purity is required for silicon wafers) was processed into pieces smaller than the gold-on-mica samples. A small drop of SU8-100 glue (negative tone photoresist, MicroChem) was added to each gold sample, and the polished surface side of the silicon pieces were placed onto the glue, then gently pressed to evenly distribute the glue between the gold and silicon. The sandwiched glue was cured at 130 ± 1°C for at least 48 hr. The samples were gradually cooled and stored at room temperature. For self-assembled monolayer (SAM) preparation, the mica was mechanically stripped from the silicon-SU8-gold sandwich to provide an ultra-flat gold surface (with a roughness of ~0.2 nm, as confirmed by AFM measurements[22]) that was immediately incubated in a thiol-containing solution (see below).

Preparation of RNA-DNA chimera sequences. A thiolated, 39-nucleotide RNA-DNA chimera sequence containing an RNase III cleavage site within the 27-nt RNA segment and a BamHI restriction site within the 12-nt DNA segment (see Seq1 below), as well as the complementary, non-thiolated [RNA-DNA] sequence (see Seq2 below) were purchased from ThermoFisher Scientific in HPLC-purified form. The DNA segments in Seq1 and Seq2 are indicated in bold-face.

Seq1: HS-$(CH_2)_6$-5′-**CAAGGATCCGAC**ACGUCAACAGACAAAAGCC-UGUACCUC-3′

Seq2: 5′-GAGGUACAGGCUUUUGUCUGUUGACGU**GTCGGATCCTTG**-3′

Preparation of ds[RNA-DNA] matrices. Self-assembled-monolayers of a pre-formed ds[RNA-DNA] chimera (1 μM) (see below) were prepared on ultraflat gold samples (see above). A solution of ds[RNA-DNA] chimera (1 μM) was prepared in TE buffer (10 mM Tris-HCl, 1 mM EDTA, pH 7.2 at 25°C; Sigma-Aldrich) in Milli-Q water (resistivity = 18.2 MΩcm) supplemented with 50 mM NaCl. The solutions were heated at 37°C for 10–15 min, then centrifuged for 1 min to collect any vapour. A fresh gold sample (see above) was incubated between 10 min and overnight[55] with the ds[RNA-DNA] chimera at room temperature. After incubation, samples were thoroughly rinsed with RNase-free, DNase-free TE buffer, pH 7.2, containing 50 mM NaCl. To block nonspecific adsorption of biomolecules, samples were incubated in 100-μM solution of 1-mercaptohexanol (Sigma-Aldrich) in TE buffer (pH 7.2) for 15 min. Samples were thoroughly rinsed with TE buffer (pH 7.2) containing 50 mM NaCl.

Nanografting of reference monolayers into ds[RNA-DNA] matrices. Nanografting[17,19,20,22,56,57] was used to prepare laterally-confined, ds[RNA-DNA] matrices. Nanografting was carried out using a Digital Instruments MultiMode AFM (Santa Barbara, CA), with a Nanoscope IIIa controller (Veeco; 12 × 12 μm scan size). All AFM experiments were carried out in solution using commercially available liquid cells. Nanografting was performed in contact mode using silicon cantilevers, such as NSC36/noAl (usually MikroMasch, tip radius <10 nm) having a spring constant between 0.9 and 1.5 N m^{-1}. Briefly, a freshly prepared ds[RNA-DNA] self-assembled monolayer was mounted in a closed fluid cell containing a 10-μM concentration of the ethylene-glycol-terminated alkylthiol, HS-$(CH_2)_{11}$-$(O\text{-}CH_2\text{-}CH_2)_6$-OH ("top-oligo-ethylene-glycol-6" (TOEG6), Sigma-Aldrich) in TE buffer with 50 mM NaCl. An AFM tip with high force loads was used to fabricate patches of TOEG6 (laterally confined SAM "pit"), in which the initially affixed molecules were locally exchanged with molecules in solution, caused by mechanical perturbation induced by the scanning tip[57]. Nanografting was carried out by applying forces of 100–200 nN, and a tip speed of ~4 μm s^{-1}. The experiments were carried out quickly (within several min) in order to prevent TOEG6 exchange through self-assembly[58] with initial SAM molecules surrounding the "pit". TOEG6 prevents the nonspecific adsorption in the pit of biomolecules used in the experiments[59].

AFM data collection. A Digital Instruments MultiMode AFM (Santa Barbara, CA) operated in contact mode with a Nanoscope IIIa controller, was used to characterize the surfaces and measure the relative topographic height of the matrices using a soft cantilever at the lowest minimal force. The softest silicon cantilevers (MikroMasch, 38-series, nominal spring constant 0.03 N m^{-1}, tip radius <10 nm) were used at a tip speed of ~5 μm sec^{-1} in 50 mM NaCl-TE buffer (pH 8.0). The absolute height of the ds[RNA-DNA] molecules (H*Abs*) was calculated as H*Abs* = H*Rel* + H*TOEGn* − H*C6*, where H*Rel* is the relative height of the ds[RNA-DNA], H*TOEGn* is the height of the TOEGn alkylthiol SAM (n = 3,6), and H*C6* is the length of the alkylthiol linker (C6-SH). H*TOEG3* = 2.3 nm, H*TOEG6* = 3.1 nm, and H*C6* = 1.0 nm[20–22,60]. The roughness (RMS) on the TOEG surfaces was measured as RMS*TOEG* ~0.2 nm. In turn, on average, H*Abs* = 1.3 ± 0.2 nm for TOEG3, and H*Abs* = 2.1 ± 0.2 nm for TOEG6, in agreement with previous studies[20–22,60]. The ds[RNA-DNA] nanopatches were imaged and recorded before and after enzyme reaction at minimal force with the soft cantilever. During imaging, the applied force load was adjusted to be as low as possible, while maintaining stable contact (typically, <2 nN). Finally, cross-sectional height profile analyses were performed on the acquired topographical images using the Nanoscope (Veeco Instruments, Version 5.12r5) in conjunction with Gwyddion software (http://gwyddion.net/). For matrices with H*Abs* > 11.5 nm it is expected that the inherent ds[RNA-DNA] density is ~10^4 μm^{-2}[20,22].

Enzyme reactions. The enzymes used in this study were *Aquifex aeolicus* ribonuclease III (RNase III) (purified as described[37]) and BamHI (obtained from New England BioLabs). *A. aeolicus* RNase III was specifically chosen for its thermostability[37]. Reactions with RNase III and the E110A RNase III mutant (see Table 1 for concentrations) were carried out at 40°C in buffer consisting of 50 mM NaCl, 15 mM $MgCl_2$, and 30 mM Tris-HCl (pH 8) (see also Table 1). BamHI was used at 0.2 U μl^{-1} (~20 nM) in conjunction with RNase III reaction buffer (see above) or the buffer supplied by the manufacturer (NEB4-buffer) (see also Table 1). The combined reactions (Input 1+: BamHI + RNase III, and Input 2+: BamHI + E110A) were performed in RNase III reaction buffer. Matrices were treated with all Inputs for 2.30 hr (unless otherwise specified). After reaction, surfaces were extensively washed with reaction buffer, followed by rinsing in 50 mM NaCl TE buffer (for RNase III or E110A) and, for combined reactions with BamHI, followed by rinsing in NEB4-buffer (100 mM NaCl, 10 mM $MgCl_2$, 50 mM Bis-Tris-HCl, 1 mM Dithiothreitol, pH 6.0 at 25°C [Sigma-Aldrich] in Milli-Q water). Immediately prior to AFM determination of H_{OUT}, all matrices subjected to Inputs 1–3, and 1–3+, were rinsed in TE buffer containing 1 M NaCl.

Ethidium bromide binding experiments. The ds[RNA-DNA] matrices were prepared as described above and subjected to height measurement. This was followed by incubation with an aqueous (5 mM) ethidium bromide solution (Sigma-Aldrich) for 15 min. Surfaces then were gently rinsed once in 50 mM NaCl TE buffer (pH 8.0), and the heights of the ss[RNA-DNA] and ds[RNA-DNA] matrices determined as described above.

Fluorescence microscopic measurements. Fluorescence measurements were performed using the Nikon Eclipse E400 microscope equipped with an Infinity2 camera. All fluorescence images were acquired using a Blue Excitation Filter Block b-2E/C (excitation filter wavelength: 465–495 nm; dichromatic mirror cut-off wavelength: 505 nm; barrier filter wavelength: 515–555 nm) at the same optical magnification and intensity exposition in order to avoid photobleaching. Fluorescence intensity profiles were obtained by ImageJ software (http://rsbweb.nih.gov/ij/).

Data analysis. Data analysis was performed using Nanoscope 5.12r5. All AFM data were analysed with Gwyddion software (http://gwyddion.net/). The Microsoft Excel (http://office.microsoft.com) processed data also was analysed using Igor Pro 6.0. graphing software (http://www.wavemetrics.com/). All colour scales used for the AFM displays shown in this work are linear.

1. Wang, D. & Bodovitz, S. Single cell analysis: the new frontier in "omics." *Trends Biotechnol.* **28**, 281–290 (2010).
2. Arlett, J. L., Myers, E. B. & Roukes, M. L. Comparative advantages of mechanical biosensors. *Nat. Nanotechnol.* **6**, 203–215 (2011).
3. Mardis, E. R. Next-generation DNA sequencing methods. *Annu. Rev. Genomics Hum. Genet.* **9**, 387–402 (2008).
4. Rothemund, P. W. K. Folding DNA to create nanoscale shapes and patterns. *Nature* **440**, 297–302 (2006).
5. Liu, J., Cao, Z. & Lu, Y. Functional nucleic acid sensors. *Chem. Rev.* **109**, 1948–1998 (2009).
6. Rajendran, A., Endo, M. & Sugiyama, H. Single-molecule analysis using DNA origami. *Angew. Chem. Int. Ed. Engl.* **51**, 874–890 (2012).
7. Husale, S., Persson, H. H. J. & Sahin, O. DNA nanomechanics allows direct digital detection of complementary DNA and microRNA targets. *Nature* **462**, 1075–1078 (2009).
8. Ray, S., Mehta, G. & Srivastava, S. Label-free detection techniques for protein microarrays: prospects, merits and challenges. *Proteomics* **10**, 731–748 (2010).
9. Garcia, R. & Herruzo, E. T. The emergence of multifrequency force microscopy. *Nat. Nanotechnol.* **7**, 217–226 (2012).
10. Ke, Y. G., Lindsay, S., Chang, Y., Liu, Y. & Yan, H. Self-assembled water-soluble nucleic acid probe tiles for label-free RNA hybridization assays. *Science* **319**, 180–183 (2008).
11. De Angelis, F. *et al.* Nanoscale chemical mapping using three-dimensional adiabatic compression of surface plasmon polaritons. *Nat. Nanotechnol.* **5**, 67–72 (2010).
12. Josephs, E. A. & Ye, T. Nanoscale positioning of individual DNA molecules by an atomic force microscope. *J. Am. Chem. Soc.* **132**, 10236–10238 (2010).
13. Hörber, J. K. H. & Miles, M. J. Scanning probe evolution in biology. *Science* **302**, 1002–1005 (2003).
14. Picco, L. M. *et al.* Breaking the speed limit with atomic force microscopy. *Nanotechnology* **18**, (2007).
15. Casuso, I. *et al.* Characterization of the motion of membrane proteins using high-speed atomic force microscopy. *Nat. Nanotechnol.* **7**, 525–529 (2012).
16. Baslan, T. *et al.* Genome-wide copy number analysis of single cells. *Nat. Protoc.* **7**, 1024–1041 (2012).
17. Stewart, M. E., Motala, M. J., Yao, J., Thompson, L. B. & Nuzzo, R. G. Unconventional methods for forming nanopatterns. *Proc. Inst. Mech. Eng. N J. Nanoeng. Nanosyst.* **220**, 81–138 (2006).
18. Liu, M., Amro, N. A., Chow, C. S. & Liu, G. Y. Production of nanostructures of DNA on surfaces. *Nano Lett.* **2**, 863–867 (2002).
19. Bosco, A. *et al.* Hybridization in nanostructured DNA monolayers probed by AFM: theory versus experiment. *Nanoscale* **4**, 1734–1741 (2012).
20. Mirmomtaz, E. *et al.* Quantitative study of the effect of coverage on the hybridization efficiency of surface-bound DNA nanostructures. *Nano Lett.* **8**, 4134–4139 (2008).
21. Castronovo, M. *et al.* Control of steric hindrance on restriction enzyme reactions with surface-bound DNA nanostructures. *Nano Lett.* **8**, 4140–4145 (2008).
22. Castronovo, M. *et al.* Two-dimensional enzyme diffusion in laterally confined DNA monolayers. *Nat. Commun.* **2**, 1–10 (2011).
23. Biagiotti, V. *et al.* Probe accessibility effects on the performance of electrochemical biosensors employing DNA monolayers. *Anal. Bioanal. Chem.* **402**, 413–421 (2012).
24. Castronovo, M. *et al.* Effects of nanoscale confinement on the functionality of nucleic acids: implications for nanomedicine. *Curr. Med. Chem.* **20**, (2013), in press.
25. Torelli, U. Characteristics of heterogeneous nuclear-RNA in normal small lymphocytes and in acute-leukemia blast cells - outline. *Acta Haematol.* **54**, 234–241 (1975).
26. Musso, M. *et al.* Double-stranded-RNA excess in hematologic diseases - clinical implications. *Haematologica* **74**, 5–9 (1989).
27. Kantarjian, H. M. *et al.* Preferential expression of double-stranded ribonucleic-acid in tumor versus normal-cells - biological and clinical implications. *Blood* **66**, 39–46 (1985).
28. Majde, J. A. Viral double-stranded RNA, cytokines, and the flu. *J. Interferon Cytokine Res.* **20**, 259–272 (2000).
29. Weber, F., Wagner, V., Rasmussen, S. B., Hartmann, R. & Paludan, S. R. Double-stranded RNA is produced by positive-strand RNA viruses and DNA viruses but not in detectable amounts by negative-strand RNA viruses. *J. Virol.* **80**, 5059–5064 (2006).
30. Colby, C. & Duesberg, P. H. Double-stranded RNA in vaccinia virus infected cells. *Nature* **222**, 940–& (1969).
31. Li, H. L. & Nicholson, A. W. Defining the enzyme binding domain of a ribonuclease III processing signal. Ethylation interference and hydroxyl radical footprinting using catalytically inactive RNase III mutants. *EMBO J.* **15**, 1421–1433 (1996).
32. Jacobs, B. L. & Langland, J. O. When two strands are better than one: the mediators and modulators of the cellular responses to double-stranded RNA. *Virology* **219**, 339–349 (1996).
33. Geiss, G. *et al.* A comprehensive view of regulation of gene expression by double-stranded RNA-mediated cell signaling. *J. Biol. Chem.* **276**, 30178–30182 (2001).
34. Munroe, S. H. & Zhu, J. Overlapping transcripts, double-stranded RNA and antisense regulation: a genomic perspective. *Cell. Mol. Life Sci.* **63**, 2102–2118 (2006).
35. Fire, A. *et al.* Potent and specific genetic interference by double-stranded RNA in Caenorhabditis elegans. *Nature* **391**, 806–811 (1998).
36. Bernstein, E., Caudy, A. A., Hammond, S. M. & Hannon, G. J. Role for a bidentate ribonuclease in the initiation step of RNA interference. *Nature* **409**, 363–366 (2001).
37. Marcus, P. I. & Sekellick, M. J. Defective interfering particles with covalently linked [±]RNA induce interferon. *Nature* **266**, 815–819 (1977).
38. Shi, Z., Nicholson, R. H., Jaggi, R. & Nicholson, A. W. Characterization of *Aquifex aeolicus* ribonuclease III and the reactivity epitopes of its pre-ribosomal RNA substrates. *Nucleic Acids Res.* **39**, 2756–2768 (2011).
39. Blaszczyk, J. *et al.* Crystallographic and modeling studies of RNase III suggest a mechanism for double-stranded RNA cleavage. *Structure* **9**, 1225–1236 (2001).
40. Calin-Jageman, I., Amarasinghe, A. K. & Nicholson, A. W. Ethidium-dependent uncoupling of substrate binding and cleavage by *Escherichia coli* ribonuclease III. *Nucleic Acids Res.* **29**, 1915–1925 (2001).
41. Murray, I. A., Stickel, S. K. & Roberts, R. J. Sequence-specific cleavage of RNA by type II restriction enzymes. *Nucleic Acids Res.* **38**, 8257–8268 (2010).
42. Halford, S. E. & Marko, J. F. How do site-specific DNA-binding proteins find their targets? *Nucleic Acids Res.* **32**, 3040–3052 (2004).
43. Li, L., Pabit, S. A., Meisburger, S. P. & Pollack, L. Double-stranded RNA resists condensation. *Phys. Rev. Lett.* **106**, (2011).
44. Mei, Q. *et al.* Stability of DNA origami nanoarrays in cell lysate. *Nano Lett.* **11**, 1477–1482 (2011).
45. Van den Hout, M., Vilfan, I. D., Hage, S. & Dekker, N. H. Direct force measurements on double-stranded RNA in solid-state nanopores. *Nano Lett.* **10**, 701–707 (2010).
46. Pinheiro, A. V., Nangreave, J., Jiang, S., Yan, H. & Liu, Y. Steric crowding and the kinetics of DNA hybridization within a DNA nanostructure system. *ACS Nano* **6**, 5521–5530 (2012).
47. Zhou, W.-J., Chen, Y. & Corn, R. M. Ultrasensitive microarray detection of short RNA sequences with enzymatically modified nanoparticles and surface plasmon resonance imaging measurements. *Anal. Chem.* **83**, 3897–3902 (2011).
48. Nicholson, A. W. Structure, reactivity and biology of double-stranded RNA, in *Progress in Nucleic Acid Research and Molecular Biology* (Cohn, W. E. C. & Moldave, K. eds) **52**, 1–65 (Academic Press, San Diego, 1996).
49. Vallée-Bélisle, A., Ricci, F., Uzawa, T., Xia, F. & Plaxco, K. W. Bioelectrochemical switches for the quantitative detection of antibodies directly in whole blood. *J. Am. Chem. Soc.* **134**, 15197–15200 (2012).
50. Liu, J.-F. *et al.* Fabrication of high-density nanostructures with an atomic force microscope. *Appl. Phys. Lett.* **84**, 1359–1361 (2004).
51. Ryan, D. *et al.* Patterning multiple aligned self-assembled monolayers using light. *Langmuir* **20**, 9080–9088 (2004).
52. Buxboim, A. *et al.* A single-step photolithographic interface for cell-free gene expression and active biochips. *Small* **3**, 500–510 (2007).
53. Bano, F. *et al.* Toward multiprotein nanoarrays using nanografting and DNA directed immobilization of proteins. *Nano Lett.* **9**, 2614–2618 (2009).
54. Melli, M., Scoles, G. & Lazzarino, M. Fast detection of biomolecules in diffusion-limited regime using micromechanical pillars. *ACS Nano* **5**, 7928–7935 (2011).
55. Peterson, A. W., Heaton, R. J. & Georgiadis, R. M. The effect of surface probe density on DNA hybridization. *Nucleic Acids Res.* **29**, 5163–5168 (2001).
56. Liu, M., Amro, N. A. & Liu, G. Y. Nanografting for surface physical chemistry. *Annu. Rev. Phys. Chem.* **59**, 367–386 (2008).
57. Liu, G. Y., Xu, S. & Qian, Y. Nanofabrication of self-assembled monolayers using scanning probe lithography. *Acc. Chem. Res.* **33**, 457–466 (2000).
58. Xu, S., Miller, S., Laibinis, P. E. & Liu, G. Y. Fabrication of nanometer scale patterns within self-assembled monolayers by nanografting. *Langmuir* **15**, 7244–7251 (1999).
59. Harder, P., Grunze, M., Dahint, R., Whitesides, G. M. & Laibinis, P. E. Molecular conformation in oligo(ethylene glycol)-terminated self-assembled monolayers on gold and silver surfaces determines their ability to resist protein adsorption. *J. Phys. Chem. B* **102**, 426–436 (1998).
60. Hu, Y. Towards Nanobiosensors: Positioning of *de novo* proteins on gold with a predictable orientation and the study of protein resistant layers. (Princeton University, Princeton, NJ, 2005).

Acknowledgements

These studies were performed in the Nicholson and MONALISA (MOlecular NAnotechnology for LIfe Science Applications) Laboratories of the Department of Biology, Temple University, Philadelphia, PA, USA, and were financially supported in part by the NIH (RO1-GM56772), the College of Science and Technology of Temple University, and the European Research Council (Grant ERC Ideas 2010 n. 269051-Monalisa's Quidproquo). The authors are grateful to Dr. Zhongjie Shi for advice and assistance with the

preparation and use of *A. aeolicus* RNase III and the E110A *A. aeolicus* RNase III mutant; to Prof. Giacinto Scoles and Prof. Flavio Maran for useful discussions on experimental design and interpretation; to Prof. Joel Sheffield for help with the fluorescence microscopy measurements; and to Prof. Giacinto Scoles and Dr. Loredana Casalis for helpful comments on the manuscript.

Author contributions

A.W.N. and M.C. conceived and designed the research. S.K.R. designed and performed the experiments and collected the data. M.C. and S.K.R. analysed the data. All authors contributed to the interpretation of the results. M.C., A.W.N. and S.K.R. wrote the manuscript, S.K.R. and M.C. wrote Materials and Methods, while all authors contributed to the revisions.

Additional information

Supplementary information accompanies this paper at http://www.nature.com/scientificreports

Competing financial interests: The authors declare no competing financial interests.

How to cite this article: Redhu, S.K., Castronovo, M. & Nicholson, A.W. Digital Imprinting of RNA Recognition and Processing on a Self-Assembled Nucleic Acid Matrix. *Sci. Rep.* **3**, 2550; DOI:10.1038/srep02550 (2013).